Combustion and Flame 181 (2017) 54–70

Contents lists available at ScienceDirect

Combustion and Flame

journal homepage: www.elsevier.com/locate/combustflame

Pressure effects on real-gas laminar counterflow

Albert Jordà Juanós*, William A. Sirignano

University of California, Irvine, CA 92697-3975, United States

ARTICLE INFO

Article history:
Received 2 June 2016
Revised 2 August 2016
Accepted 21 January 2017

Keywords:
Counterflow
Diffusion
Supercritical
Methane hydrates
Chemical equilibrium

ABSTRACT

Two important problems are studied: the combustion of hydrocarbons at higher pressures and the burning of hydrocarbon/water-vapor mixtures both of which are relevant to many applications including diesel combustion and hydrate fuels. To study both of these problems, a numerical analysis of a steady laminar methane-air counterflow diffusion flame at high pressure is presented. The mathematical model is based on the well-known similar solution for counterflow with special considerations given to the high density and to detailed transport and chemistry. Modifications of transport properties and associated time scales with increasing pressure are considered. Real gas behavior is examined through the use of a cubic equation of state and an enthalpy departure function. A more complete version of the energy equation is presented. The effects on flame structure, location, and peak temperature are analyzed for a range of pressure from 1 to 100 atm. Assessment of the different high-pressure corrections indicate that introduction of the cubic equation of state is the most profound adjustment, while the correction of transport properties is the least significant. The use of the enthalpy departure function is important. The flame structure and heat-release rate are confirmed to follow previously identified correlations with the pressure-weighted strain rate. Extinction occurs when the mass fraction of H_2O vapor in the methane stream is greater than 67% and the mixture impinges against air. Small differences in results occur between the classical chemical equilibrium employing partial pressures versus the non-ideal formulation that uses fugacities. The Soret effect and radiative heat losses are shown to be negligible, even at the highest pressures. An order of magnitude analysis shows that turbulence generation is practically inconsequential.

1. Introduction

The present study will give similar solutions that provide reliable conclusions about the laminar steady axisymmetric counterflow diffusion flame structure and location at very high pressures. An application of these solutions is found, for example, in the flamelet model for turbulent flames. Combustion under high pressures leads to an increase in both thermodynamic and fuel efficiencies as well as reduced emission of some pollutants. These advantages are causing the current trend towards burning at high-pressure regimes. For instance, aircraft gas turbine engines now operate at ~ 30 atm, a value that has been increasing at a near linear rate for more than 50 years and is expected to continue to do so [1]. Another example is that of diesel engines, which obtain pressures as large as ~ 60 atm after ignition [2–6]. In many rocket engines, one of the reactants is injected in a liquid form at a temperature which is below the critical value but at supercritical pressure. These conditions were named as transcritical [7] and the pressure takes values which are typically of the order of 100 atm but may reach levels as high as 400 atm [8–10].

Ideal-gas approximations are often considered in combustion problems with the argument that at high temperatures and low densities the compressibility factor will be close to unity. At very high pressures, however, this may not necessarily be true. It is the responsibility of any analyst treating these high-pressure flows to justify the ideal-gas approximation. In our study, we present results for a canonical combustion configuration with both ideal and real-gas models for comparison purposes and error estimation.

Another motivation for the present study is combustion at high pressures where the fuel is a mixture of methane and water vapor in relation to gas hydrates. These materials are ice-like crystalline solids formed from a network of hydrogen-bonded water molecules that encapsulate guest gas molecules [11]. There is a significant amount of methane naturally stored in the form of methane hydrates, also known as methane ice or methane clathrates. Sediment containing methane hydrates is found within specific pressure-temperature conditions that occur in regions of permafrost and beneath the sea in outer continental margins at depths of the order of a thousand meters [12] where pressure reaches the value of 100 atm. It is not in the scope of this study

* Corresponding author.
E-mail address: ajordaju@uci.edu (A. Jordà Juanós).

http://dx.doi.org/10.1016/j.combustflame.2017.01.030
0010-2180/

to determine whether combustion of methane hydrates in their natural conditions is practical. Rather, it poses an interesting problem from which conclusions can be extracted for a broader range of applications, including rocket engines, bio-fuels, direct water injection, or exhaust gas recirculation (EGR) in engines. For a detailed description of methane hydrate combustion, the reader is referred to [13].

The literature on counterflow diffusion flame problems is broad and continues to expand. It includes analytical, experimental and numerical approaches [14,15]. Such flames are of fundamental interest because they approximate a one-dimensional character and because residence times within the flame zone can be easily varied [16]. This laminar flame has also been proposed as a key element in the complex structure of turbulent nonpremixed flames [17].

Even though most of the literature deals with situations at atmospheric pressure and ideal-gas conditions, some recent papers used numerical methods to examine flame characteristics entailing real-gas formulations to account for the high-pressure effects. Also, most specific examples are for oxygen/hydrogen systems, with less attention being given to hydrocarbons. For instance, an O_2/H_2 system was explored to find a correlation between the flame thickness and heat-release rate with the pressure-weighted strain rate [18]. Flame instabilities were studied in [19] using a flamelet model. Detailed investigation of the extinction strain rates appeared later for counterflow diffusion flames at subcritical and supercritical conditions for oxygen/hydrogen mixtures [20] and for oxygen/n-alkane hydrocarbons [21]. These papers identified general similarities in the mixture-fraction space in terms of flame temperature, species concentrations, flame thickness, and heat-release rate, suggesting that the flame behaviors at high pressure can be evaluated by their counterpart at low pressure. With regard to the n-alkane family of fuels, similarities indicated that flame properties of a given hydrocarbon can be predicted from those of another hydrocarbon at the same flow conditions.

Counterflow diffusion flame experimental studies at atmospheric pressure are common. For instance, results of an axisymmetric configuration with methane and enriched air were compared to computational solutions obtained from both one-dimensional and two-dimensional mathematical models [22]. The comparison between the experimental and computational data yielded excellent agreement for all measured quantities. Studies of the same kind at elevated pressures are unconventional, but some exist. See, for example, [23–25] for pressures up to 2.5 MPa.

The literature also includes studies with regard to the presence of water premixed with the fuel stream at atmospheric pressure. An experiment [26] was conducted under microgravity conditions to study the influence of water mists on premixed flames propagating in a cylindrical tube. Results showed that the flame speed initially increases due to the thermal expansion of combustion gases with higher water content, while a later decrease in flame speed is caused by heat removal, mixture dilution, and radical recombination. A numerical counterflow analysis was presented, where air was introduced on one side and a preheated mixture of water vapor/methane entered on the other side [27]. Extinction limits were explored and compared with experimental results. Agreement was found for suitable fuel and oxidizer flow rates. Extinction occurred with lower water content compared to experiments when simulations were performed at higher flow rates, revealing the influence of strain rate. In another study, the dilution extinction limits of $H_2 - O_2$ diffusion flames were assessed by mixing water with the fuel, where H_2O modeled combustion products [28]. Other reasons for water injection into the combustion chamber include decreasing exhaust temperature and associated NOx emissions, flame extinguishment, or studying combustion efficiency [29–32].

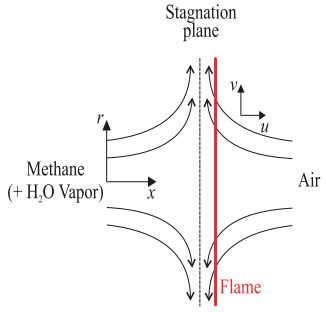

Fig. 1. Non-premixed counterflow axisymmetric configuration.

In comparison with the reviewed literature, the current study contributes in several significant new aspects: (1) a real-gas model that entails fewer simplifying assumptions than previous studies (a more complete energy equation with the associated enthalpy correction for mixtures is presented and evaluated); (2) evaluation of the effects of various high-pressure corrections and determination of their relative importance; (3) evaluation of the correct use of fugacities as opposed to partial pressures in chemical-equilibrium calculations; (4) quantification of the radiative heat losses at high pressure; (5) evaluation of the Soret effect at high pressure; (6) analysis of turbulent kinetic energy generation due to shear in the stagnation plane; (7) extension of scaling rules to higher pressures; and (8) analysis of the effects of introducing water vapor in the fuel stream at high pressure. To the best of the authors' knowledge, points 1 through 7 have not been done before. Point 8 has been done for a $H_2 - O_2$ flame [28], but not for methane and air at high pressures in relation to the methane hydrates and other applications.

In Section 2, we review the mathematical model that we use in our study. The equation of state is discussed in Section 3. The method of solution, validation, and results are presented in Sections 4, 5, and 6, respectively. Supporting information on chemical equilibrium is presented in Appendix A.

2. Model

Figure 1 shows a sketch that represents the axisymmetric flow between two circular opposed jets and the flame that is generated. Pure methane or a mixture of methane with water vapor flows from the left nozzle while air flows from the right nozzle. Under the boundary-layer approximation, the two-dimensional problem may be simplified to a system of ODEs with the independent variable that is the x-coordinate normal to the stagnation plane [33,34]. Slightly different formulations are available, depending on which parameter is chosen to alter the strain. Prescribing the momentum fluxes at the exit of the nozzles fixes the radial pressure gradient and the strain rate of the problem, or vice versa. The approach described in [34] is followed with modifications in the energy equation and the equation of state.

The governing equations are summarized below, starting with the steady-state continuity equation in cylindrical coordinates.

$$\frac{\partial(r\rho u)}{\partial x} + \frac{\partial(r\rho v)}{\partial r} = 0. \tag{1}$$

The stream function is introduced as $\Psi(x, r) \equiv r^2 F(x)$, which satisfies the steady-state continuity equation exactly if

$$\frac{\partial \Psi}{\partial r} = r\rho u = 2rF \; and \; -\frac{\partial \Psi}{\partial x} = r\rho v = -r^2 \frac{dF}{dx}. \tag{2}$$

Then, the axial velocity u depends only on x and the radial velocity v varies linearly in r. The temperature T and species mass fractions Y_k are also functions of x only. Using the small Mach number approximation, the thermodynamic pressure p is assumed

to be constant in the equation of state but pressure-gradient terms are allowed in the momentum equations, where the term $d(r\tau_{rr})/dr$ associated with the stress in the radial direction is neglected from the boundary-layer analysis. The pressure gradient in the axial direction is zero at the stagnation point, even without taking any boundary-layer approximation. Furthermore, the Navier–Stokes equations are satisfied exactly at that point. This is a classic result for stagnation-point flow. Away from the stagnation point, but still in the central streamline, the pressure gradient is of the order of Mach number squared (M^2). Also, we have that $M << 1$, given that the flow speed will be at most 1 m/s, and the speed of sound will be around 340 m/s in the worst case scenario. Therefore, the pressure gradient in the axial direction is negligible, and the stagnation pressure, which will be the same on either side of the stagnation plane, will also be essentially the same at the boundaries.

With these considerations and neglect of body forces, the momentum equations reduce to third-order ordinary differential equations. From these equations, an eigenvalue independent of x appears: $H = r^{-1}dp/dr$.

Define the function $G(x) = dF/dx$. Then, the radial momentum equation becomes a 2nd-order ODE rather than one of 3rd order,

$$H - 2\frac{d}{dx}\left(\frac{FG}{\rho}\right) + \frac{3}{\rho}G^2 + \frac{d}{dx}\left[\mu\frac{d}{dx}\left(\frac{G}{\rho}\right)\right] = 0, \tag{3}$$

where μ is the viscosity.

The species continuity equation is

$$2F\frac{dY_k}{dx} + \frac{d}{dx}(\rho Y_k V_k) - W_k\dot{\omega}_k = 0 k = 1, 2, \ldots, K, \tag{4}$$

where the index k identifies each species and K is the total number of species.

The energy equation for non-ideal gases is

$$2F\left(\frac{dh}{dx} - \sum_{k=1}^{K} h_k\frac{dY_k}{dx}\right) - \frac{d}{dx}\left(\lambda\frac{dT}{dx}\right) + \rho\sum_{k=1}^{K} Y_k V_k\frac{dh_k}{dx} + \sum_{k=1}^{K} W_k h_k\dot{\omega}_k = 0, \tag{5}$$

where λ is the thermal conductivity, h is the mixture specific enthalpy, h_k is the species specific enthalpy, W_k are the species molecular weights and $\dot{\omega}_k$ is the rate of consumption. Both h and h_k are computed from fundamental thermodynamic theories as the summation of the ideal-gas enthalpy plus a departure function that accounts for dense fluid effects (see Section 3). It includes both the heat of formation and the sensible enthalpy. Heat losses due to radiation are neglected. Below, we confirm their minor importance compared to the energy conversion rate and heat conduction rate. (See Section 5.) For ideal gases, Eq. (5) reduces to

$$2Fc_p\frac{dT}{dx} - \frac{d}{dx}\left(\lambda\frac{dT}{dx}\right) + \rho\frac{dT}{dx}\sum_{k=1}^{K} c_{p_k}Y_k V_k + \sum_{k=1}^{K} W_k h_k\dot{\omega}_k = 0, \tag{6}$$

where c_p is the specific heat at constant pressure. The viscosity μ and thermal conductivity λ are to be evaluated both with ideal gases and with empirically correlated functions that were developed to extend kinetic gas theory to include dense fluids [35].

V_k is the diffusion velocity and it is evaluated using the multicomponent formulation [16], in which pressure effect has been neglected.

$$V_k = \frac{1}{X_k\overline{W}}\sum_{j=1}^{K}\mathcal{D}_{kj}W_j\frac{dX_j}{dx} - \frac{\mathcal{D}_k^T}{\rho Y_k}\frac{1}{T}\frac{dT}{dx}. \tag{7}$$

X_k are the species mole fractions, $\overline{W}$ is the mean molecular weight, $\mathcal{D}_{kj}$ are the ordinary multicomponent diffusion coefficients, and $\mathcal{D}_k^T$ are the thermal-diffusion coefficients. Ideal gas thermodynamic and transport properties, as well as the reaction rates are obtained from the library of subroutines in Reaction Design's Chemkin software. The second term on the right hand side of Eq. (7), also known as Soret effect, is in general neglected. However, for comparison purposes, we perform a check including this effect for one of our cases at 100 atm (see the discussion in Section 6.3 and Fig. 11).

A simplified version of Eq. (5) results from the approximation that the enthalpy of the mixture $h = \sum_k Y_k h_k$ in the convective term.

$$2F\sum_{k=1}^{K} Y_k\frac{dh_k}{dx} - \frac{d}{dx}\left(\lambda\frac{dT}{dx}\right) + \rho\sum_{k=1}^{K} Y_k V_k\frac{dh_k}{dx} + \sum_{k=1}^{K} W_k h_k\dot{\omega}_k = 0. \tag{8}$$

Eq. (8) has been used in the literature as a real-gas model [10,18,20,21]. However, the underlying assumption is that $h = \sum_k Y_k h_k$, which is not necessarily satisfied when dealing with real gases.

The three forms of the energy equation (Eqs. (5), (6), and (8)) are employed in this study for comparison purposes.

The eigenvalue $H = constant$, the function $G = dF/dx$, Eqs. (3) and (4), together with the energy equation and the equation of state (see Section 3), form a well-posed boundary-value problem, where the unknowns are H, F, G, Y_k, T and ρ. For the given chemical mechanism involving K species, the total number of differential equations is $K+3$ and the number of difference equations is $N(K+3)$, where N is the number of grid points. Plug-flow boundary conditions are specified at the exit of the nozzles. As described in [36], these conditions can be reproduced accurately in laboratory experiments. In the following, F and O stand for fuel and oxidizer, respectively. At $x = 0$:

$$F = \frac{\rho_F u_F}{2},\ G = 0,\ T = T_F,\ Y_k = (Y_k)_F. \tag{9}$$

At $x = L$:

$$F = \frac{\rho_O u_O}{2} = -\frac{\rho_F u_F}{2},\ G = 0,\ T = T_O,\ Y_k = (Y_k)_O. \tag{10}$$

We prescribe $u_F = 1$ m/s. The mass flux at $x = L$ is set to be equal in magnitude to the mass flux at $x = 0$ with opposite sign. Thus, u_O is also prescribed. Previous articles such as [20,21] match the momentum fluxes instead of mass fluxes. The choice is arbitrary and the consequences are mild as shown in Appendix B. In our study, the Reynolds number in the vicinity of the stagnation plane layer is, at most, of the order of 10^4. Later, we explain how turbulence can be avoided. (See Section 5.)

With regard to chemical kinetics, the detailed reaction mechanism GRI 3.0 [37] is selected, which consists of $K = 53$ species and 325 elementary reactions. Available reaction mechanisms were developed at relatively low pressures. These mechanisms bring the species into chemical equilibrium, which in the classical form is based on partial pressures. At elevated pressures, however, chemical equilibrium is based on fugacities. We perform a check in Appendix A and validate that the differences are small. An unresolved concern arises with the use of existing chemical kinetic mechanisms (pathways) at very high pressures, since there is a lack of experimental validation.

3. Equation of state

The Soave–Redlich–Kwong Equation of State (EoS) is selected because of its reasonable accuracy for a wide range of fluid states [38].

$$p = \frac{R_u T}{v - b} - \frac{a}{v(v+b)}. \tag{11}$$

This empirical equation, which may be rearranged to a cubic form with regards to the molar volume v, has two parameters

a and b, which are constants for single-component fluids, but become composition, pressure, and temperature dependent in the multicomponent version. The cubic form in terms of the compressibility factor Z is

$$Z^3 - Z^2 + (A - B - B^2)Z - AB = 0, \tag{12}$$

where

$$Z \equiv \frac{pv}{R_u T} \quad ; \quad A \equiv \frac{ap}{(R_u T)^2} \quad ; \quad B \equiv \frac{bp}{R_u T}. \tag{13}$$

The parameter mixing rules of the Soave–Redlich–Kwong EoS are employed [39]:

$$a = \sum_{i=1}^{K}\sum_{j=1}^{K} X_i X_j (a_i a_j)^{0.5}(1 - k_{ij}) \quad ; \quad b = \sum_{i=1}^{K} X_i b_i. \tag{14}$$

The pure species attractive and repulsive parameters a_i and b_i may be obtained from the species critical points as

$$a_i = a_{ci}\alpha_i \quad ; \quad a_{ci} = 0.42748\frac{(R_u T_{ci})^2}{P_{ci}} \quad ; \quad \alpha_i^{0.5} = 1 + S_i(1 - T_{ri}^{0.5})$$
$$S_i = 0.48508 + 1.5517\omega_i - 0.15613\omega_i^2 \quad ; \quad b_i = 0.08664\frac{R_u T_{ci}}{P_{ci}}, \tag{15}$$

where T_{ci} and P_{ci} are the critical temperature and critical pressure of mixture component i, k_{ij} is the characteristic binary interaction constant and ω_i are the acentric factors. These values are taken from the literature [40]. Sub-index r stands for "reduced" and equals the property temperature or pressure divided by its critical value. All the attractive and repulsive parameters of chemically stable species such as H_2, O_2, N_2, H_2O, or metastable species like H_2O_2, may be determined from critical states conditions. However, chemically unstable species such as radicals do not have associated critical states, thus not allowing straightforward calculation of their attractive and repulsive terms. Assuming that the ith species is a Lennard–Jones gas, for instance, it is possible to estimate the critical volume $v_{c,i}$ and the critical temperature $T_{c,i}$ [41] and to obtain that

$$a_i = (5.55 \pm 0.12)n\epsilon_i\sigma_i^3 \quad ; \quad b_i = (0.855 \pm 0.018)n\sigma_i^3, \tag{16}$$

where n is the Avogadro number, σ_i and ϵ_i are the molecular diameter and Lennard–Jones potential well depth of the ith species, respectively.

The specific enthalpy departure function is given by

$$h - h^* = \frac{1}{\overline{W}}\left\{R_u T(Z-1) + \int_\infty^v \left[T\left(\frac{dP}{dT}\right)_v - P\right]dv\right\}, \tag{17}$$

where h^* is the enthalpy for an ideal gas at the given temperature and with the same composition. This departure function can be determined using the EoS [42]:

$$h - h^* = \frac{1}{\overline{W}}\left[R_u T(Z-1) + \frac{T\frac{da}{dT} - a}{b} ln\frac{Z+B}{Z}\right]. \tag{18}$$

The species specific enthalpy h_k is also evaluated using Eq. (18), where the mixture parameters are replaced by those corresponding to the individual species.

4. Solution method

A new simulator program has been written, which contains the mathematical model and boundary conditions. The differential equations are discretized using conventional finite-differencing techniques for nonuniform mesh spacing. Central differences are used for diffusive terms, with truncation error that is second-order. For better convergence, convective terms are discretized with upwind differencing, using the sign of the velocity to choose in which direction the spatial difference should go. For such terms, the truncation error is of first-order, leading to what is often called "artificial diffusion", but this form avoids unwanted oscillations during the solution on a coarse mesh. The simulator program calls the boundary-value problem solver TWOPNT [43] to determine the steady-state solution. In the counterflow-diffusion-flame problem, the cost of forming and factoring the Jacobian matrix can be very expensive. For this reason, TWOPNT is based on a modified Newton's iteration method in which the Jacobian matrix is retained through several steps and re-evaluated only periodically. The iteration process begins from a solution guess with a coarse mesh. When a steady-state solution is found for a particular mesh, TWOPNT constructs a succession of finer grids with more points located where the solution changes abruptly until mesh independence is achieved. The criterion that determines grid independence (defined in [43]) is based on two tolerance values chosen by the user. We used 0.5 for both. If the steady-state search fails, TWOPNT undertakes a transient evolution solely to replace the starting guess by a better estimate. The evolution here is a pseudo-transient process, valuable only for producing the steady asymptote. The following time-dependent terms are added to the left side of the momentum, energy and species equations, respectively:

$$\text{Momentum: } \frac{dG}{dt}, \text{ Species: } \rho\frac{dY_k}{dt}, \text{ Energy: } \rho\frac{dh}{dt} - \sum_K \rho h_k \frac{dY_k}{dt}. \tag{19}$$

The transient term used with the simplified forms of the energy equation (Eqs. (6) and (8)) is $\rho c_p \frac{dT}{dt}$.

Note that the true transient equations would have a time derivative in the continuity equation, thereby disallowing the creation of a stream function until a steady-state is reached. However, these pseudo-transient equations still give asymptotically the steady state while allowing a stream function to be created during the transient period.

Simulations at higher pressures can present convergence difficulties. So, when the pressure is increased, the solution of a previous case at a lower pressure is employed as the initial guess.

5. Verification and validation

In order to validate our code, temperature profiles have been compared against experimental data at the highest possible pressure values. Temperature profiles are taken from [23] at 0.2, 0.4 and 0.8 MPa. We ran simulations with the same boundary conditions and domain size, entailing our most complete set of high-pressure corrections. As shown in Fig. 2, there is good agreement between our computations and the experimental results.

Validation at 100 atm is also presented against numerical results from [21] for a methane-oxygen system where the strain rate is 1000 s^{-1}. Figure 2b highlights a small difference in peak temperature. The source of this deviation could be due to the use of different chemical kinetic s schemes or the different sub-models. To answer this question, we obtained a solution with our model and a reduced chemical kinetic mechanism that entails 19-species and 15 steps[44]. The curves belonging to our detailed and reduced chemistry sets are practically superimposed. The peak temperature resulting from the use of reduced chemistry is only 4 K hotter than for detailed chemistry, while the peak temperature in [21] is 60 K hotter than our detailed kinetics result. Thus, the deviation from [21] cannot be explained by the use of different chemical kinetic schemes and is primarily diffusion controlled.

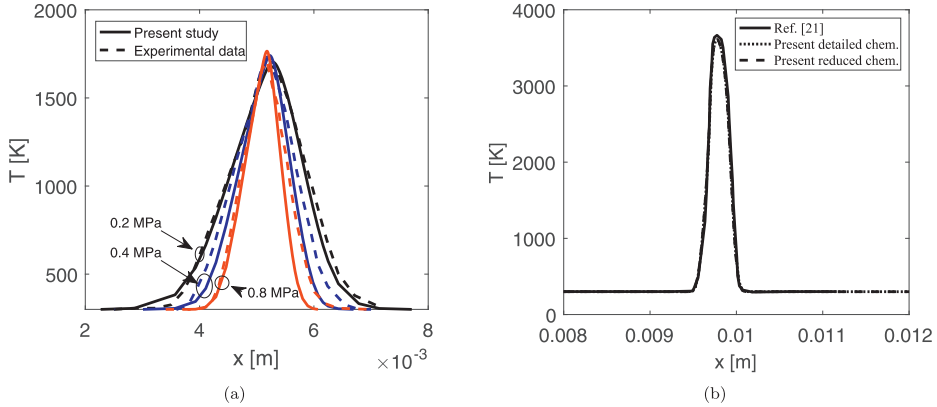

Fig. 2. (a) Temperature profile benchmarking with [23]; (b) Benchmarking with [21] for a $CH_4 - O_2$ system at 100 atm.

Consequently, our additional correction makes a modest difference at the given strain rate.

As mentioned in the Model section, a check on the importance of radiative effects was performed. To this effect, we estimated the radiative heat rate and compared it with the energy conversion rate and the conductive heat rate. The calculations on radiation are based on a method published elsewhere [45]. The radiative heat loss is computed as $q_{rad} = \sum_{k=1}^{K} p_k \kappa_k \sigma (T^4 - T_b^4)$, where p_k is the partial pressure, κ_k is the Planck mean absorption coefficient for species k, σ is the Stefan–Boltzmann constant, and T_b represents the temperature of the background environment (300 K). The Planck mean absorption coefficients depend on the species and temperature. They are taken from 5th degree Gaussian curve fittings reported in [45]. Four species (CO_2, H_2O, CO, NO) are used. The results are illustrated in Fig. 3, which shows a blow up of the heating zone from Case 6 (real-gas model without water, see Section 6) at a pressure of 100 atm.

Figure 3a shows temperature and three black curves that represent conductive heat rate (solid), radiative heat rate (dotted), and energy conversion rate (dashed). The energy conversion rate and heat rate by conduction are practically matched. The radiation curve is on the zero line. Figure 3b highlights the small magnitude of the radiative rate compared to conduction and conversion. Figure 3c and d display the same quantities for Case 8c (real-gas model with the highest studied water content, see Section 6), also at a pressure of 100 atm. The radiative heat rate is now greater than it was for Case 6, but its value is still two orders of magnitude below the other two energy rates. Thus, we conclude that radiation can be neglected.

Let us discuss how the flow can remain laminar even at the high Reynolds number at high pressures. We identify four potential sources of turbulence: (i) turbulence coming from the interior of the two burner ducts; (ii) buoyancy instability; (iii) turbulence being generated in the shear layer of the gas jet; and (iv) turbulence being generated in the shear layer near the stagnation plane region. See the sketch presented in Fig. 4a where these four regions have been highlighted. Below we review each one of these turbulence sources.

(i) We can assume that the nozzles are equipped with suitable porous materials or very fine grids such that any eddies entering from the nozzles would decay in a very short distance after entering the studied domain.

(ii) A discussion on the appearance of instabilities due to buoyancy is presented in [36]. The authors report that special care is needed to produce turbulence when it is needed. They also note that laminar flow has been obtained at 25 atm and laminar behavior at higher pressures can be expected if the layer with density variation has its thickness decreasing as $p^{-2/3}$ or faster. See Fig. 4b, which shows the variation of flame thickness for Case 6 in this study (solid), the variation with $p^{-1/2}$ (dotted, from the literature), and the variation with $p^{-2/3}$ (dashed). There is no significant difference between the three curves in terms of order of magnitude. Hence, we can also assume very little instability will appear from source (ii).

(iii) Turbulence generated in the outer shear layer of the jet may be avoided with the use of a co-flow, which in fact is a common practice in actual experiments.

(iv) To justify our neglect of turbulence from this fourth source, we include an order of magnitude analysis using a well-established equation for the calculation of the advective flux, diffusion, generation, and dissipation of turbulent kinetic energy in a shear-layer. The equation is taken from [46]:

$$\rho \frac{Dk}{Dt} = -\frac{\partial}{\partial y}(\rho \overline{v'k} + \overline{v'p'}) - \rho \overline{u'v'} \frac{\partial u}{\partial y} - \sum \left(\frac{\overline{\partial u_i'}}{\partial x_j} \right)^2 . \quad (20)$$

The three terms on the right hand side represent diffusion, production, and dissipation, respectively. We identified that the production term is dominant with respect to dissipation. So, we look at the worst case scenario where only production plays a role. We have that $(\overline{u'v'}) = \mathcal{O}(k)$ which arbitrarily maximizes production rate by assuming that both velocity components have comparable magnitudes and the fluctuation velocity components are well correlated. $\partial u/\partial y$ in our coordinate system is $\partial v/\partial x$. We obtain the order of magnitude of this quantity from the solution of Case 6 at 100 atm. Taking the order of magnitude of the radial direction as $\mathcal{O}(r) = 10^{-2}$ m, we get from Fig. 5 that $\mathcal{O}(\partial v/\partial x) = 10^5 \mathcal{O}(r) = 10^3$ s^{-1}.

Therefore, a rough but conservative estimate neglecting any decrease in k due to diffusion or dissipation yields

$$\frac{1}{k}\frac{\Delta k}{\Delta t} = \mathcal{O}(10^3 s^{-1}). \quad (21)$$

We obtain the characteristic flow time in the radial direction by dividing the radii of 1 cm by the characteristic velocity of 1 m/s. Hence, $\Delta t = \mathcal{O}(10^{-2}$ s). With this, we get the order of magnitude in the change of turbulent kinetic energy along the radial direction near the stagnation plane:

$$\frac{\Delta k}{k} = \mathcal{O}(10). \quad (22)$$

The maximum mean velocity in the radial direction is of the order of 1 m/s, but it is much smaller near the stagnation point,

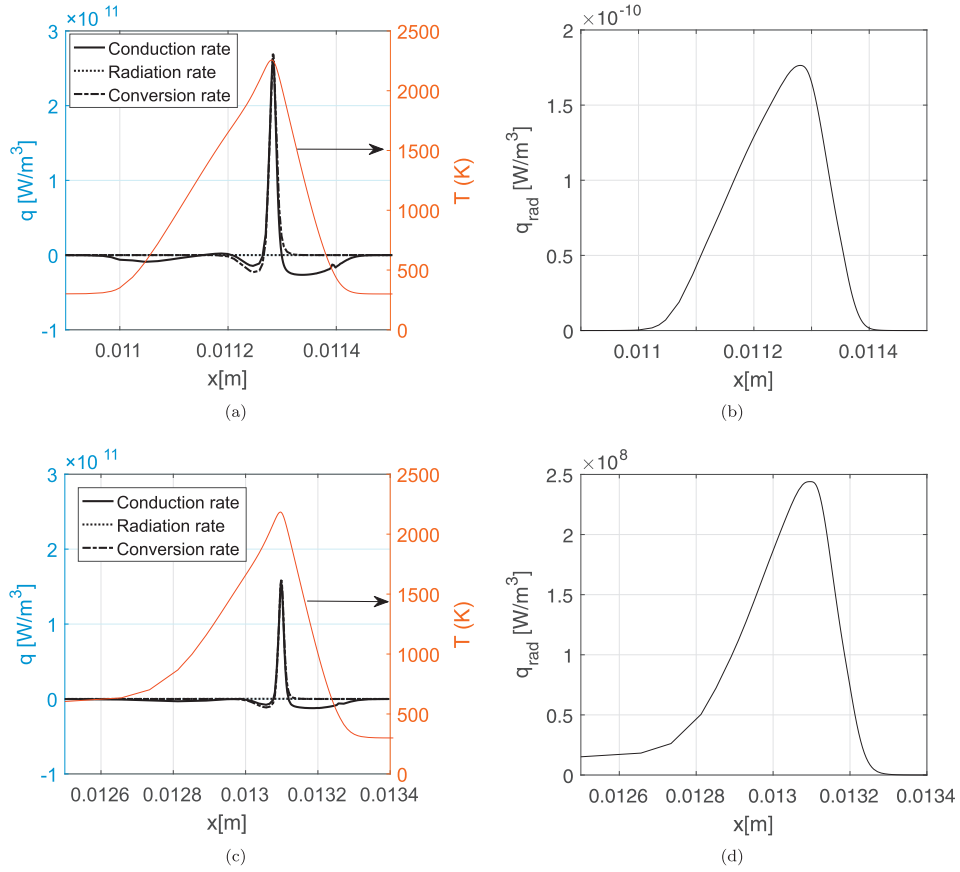

Fig. 3. Comparison of radiation, conduction, and energy conversion rates at 100 atm for Case 6 in (a) and (b), and Case 8c in (c) and (d).

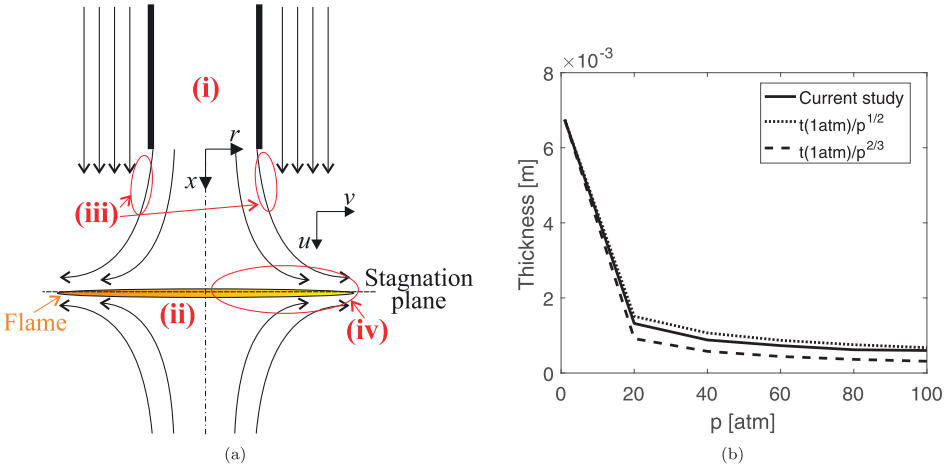

Fig. 4. (a) Turbulence sources; (b) Thickness of the layer with density variation vs. *T*.

which is the starting region for this class of turbulence. We take for this region the magnitude $\bar{v} = \mathcal{O}(0.1$ m/s). The velocity fluctuation for fully developed turbulent flow is of the order of 5–10% of the mean velocity. However, near the stagnation point, turbulence only will start being generated. So, we could estimate that the velocity fluctuation $v' = \mathcal{O}(10^{-3}$ m/s) or less in that region near the flow axis. That is, we take the velocity fluctuation in that stagnation region to be an order of magnitude less than the local value for fully developed turbulence. Thus, the turbulent kinetic energy near the stagnation point is $k = \mathcal{O}(10^{-6}$ m^2/s^2). At r=1 cm, our previous estimate yields $k = \mathcal{O}(10 * 10^{-6}) = \mathcal{O}(10^{-5}$ m^2/s^2). k increases tenfold, therefore, the velocity fluctuation increases about threefold. At r=1 cm: $v' = \mathcal{O}(3 * 10^{-3}$ m/s) and $\bar{v} = 1$ m/s.

This analysis shows that the velocity fluctuation in the radial direction is two-to-three orders of magnitude below the mean velocity, even when dissipation and diffusion away from the production region are not considered. For our problem, we deem the laminar flow assumption valid because turbulence is essentially not being generated to any meaningful extent.

Table 1
Studied cases.

Case	Correction I: EoS	Correction II: energy equation	Correction III: μ and λ
1	Ideal	Ideal (Eq. (6))	Ideal
2	Ideal	Ideal (Eq. (6))	Corrected
3	Cubic	Ideal (Eq. (6))	Ideal
4	Ideal	Corrected (Eq. (5))	Ideal
5	Cubic	Corrected (Eq. (5))	Ideal
6	Cubic	Corrected (Eq. (5))	Corrected
7	Cubic	As in literature (Eq. (8))	Corrected
8a	Equivalent to Case 6 – fuel inlet contains 10% water vapor.		
8b	Equivalent to Case 6 – fuel inlet contains 20% water vapor.		
8c	Equivalent to Case 6 – fuel inlet contains 40% water vapor.		

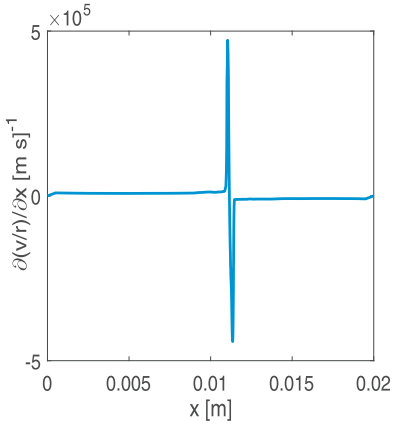

Fig. 5. Derivative in the axial direction of v/r.

6. Results

Eight cases are studied as defined in Table 1, each with varied pressure from 1 to 100 atm. The distance between the two nozzles is $L = 2$ cm, similar to what is used in typical experiments. Pure methane flows against air in Cases 1–7, where the temperature at both boundaries is 300 K, and the fuel inflow velocity equals to 1 m/s. The air nozzle flow speed is calculated according to the F boundary condition (see Eq. (10)). As mentioned in the Introduction section, one of our goals is to determine the relative importance associated with high-pressure rectifications. Differences across Cases 1–7 reflect three real-gas corrections: (I) replacement of the ideal-gas law by the cubic equation of state; (II) use of the real-gas energy equation (Eq. (5)); and (III) modification of the viscosity and thermal conductivity.

No corrections are used in Case 1. Only the transport properties are corrected in Case 2. Case 3 is equipped with the cubic EoS and no other corrections. Case 4 entails the real-gas energy equation (Eq. (5)), ideal-gas law, and no transport modification. A combination of corrections (I) and (II) are used in Case 5, while Case 6 presents all three corrections. Case 7 is used to study the error introduced by assuming that the enthalpy of the mixture equals the summation of the enthalpy of each component times its mass fraction in the energy equation. Namely, it uses a more simplified version of the energy equation (Eq. (8) as presented in previous studies [10,18,20,21] instead of Eq. (5)).

In addition, Case 8 is used to study the effect of water vapor content premixed with the methane in the fuel stream. All high-pressure corrections are enabled in this case. The temperature at the exit of the fuel stream is raised to 600 K, a value that is above the saturation temperature of water at 100 atm. See Table 1 for a summary of these cases.

The comparative study between Cases 1 and 6 is shown in Section 6.1. The effects of the new enthalpy approach in the energy equation are discussed in Section 6.2. Results and discussion of the cases entailing the most complete physical model with and without premixed water vapor (Cases 6 and 8) are shown in Sections 6.3 and 6.4.

6.1. Comparing Cases 1–6

To better assess the effects of the three corrections, solutions for Cases 1–6 at 100 atm are plotted together in Figs. 6 and 7. For a given pressure, temperature, composition, and fuel-inlet velocity, the most accurate mass flow rates at the boundaries are given by the real-gas model. Use of simplified models such as the ideal-gas law, yield a less accurate density value at the boundaries which of course affects the mass flow rates. The choice here is arbitrary: (i) either keep the fuel-inlet velocity, temperature, pressure, and composition fixed at the boundaries and only change the model; or (ii), if we wanted to keep the mass flow rates the same when comparing between ideal and real models, we would have to modify the temperature, pressure, or composition such that the density at the boundaries matched between real and ideal models. (Or we must change the inlet velocity which would affect the strain rate.) We chose the former approach (i) because they present as the given parameters the more easily measurable quantities. As mentioned above, we prescribe the velocity at the exit of the fuel nozzle and match the mass flow rates of the two nozzles. Note that under the latter approach (ii), we would be studying two different problems.

Figure 6a, b, and d show two groups of almost overlapped curves, one containing Cases 1, 2, 4 and the other including Cases 3, 5 and 6. These figures show the whole domain. A narrower domain is shown in the rest of the figures to gain resolution. A closer look at the velocity profiles shows that the correction in transport properties has a very small effect on the solutions. In contrast, application of the cubic equation of state introduces a substantial difference, which moves the flame and stagnation coordinate closer to the center plane. Correction of the energy equation causes more change than transport correction, but is less significant than replacing the equation of state. Furthermore, it moves the stagnation plane away from the center of the domain.

Figure 6d shows the function G, which is related to the radial velocity v. The curves exhibit an almost linear behavior for most of the domain except for a thin layer around the flame. We can see a substantial change in the slope of the linear part of the curves for the cases entailing the cubic equation of state.

Analysis of Fig. 6e and f shows that substantial changes in density occur due to the variation in compressibility factor with respect to unity, specially on the fuel side. Indeed, when we look at Fig. 6f, we see that methane density is significantly higher for cases with the cubic equation of state (3, 5 and 6), which

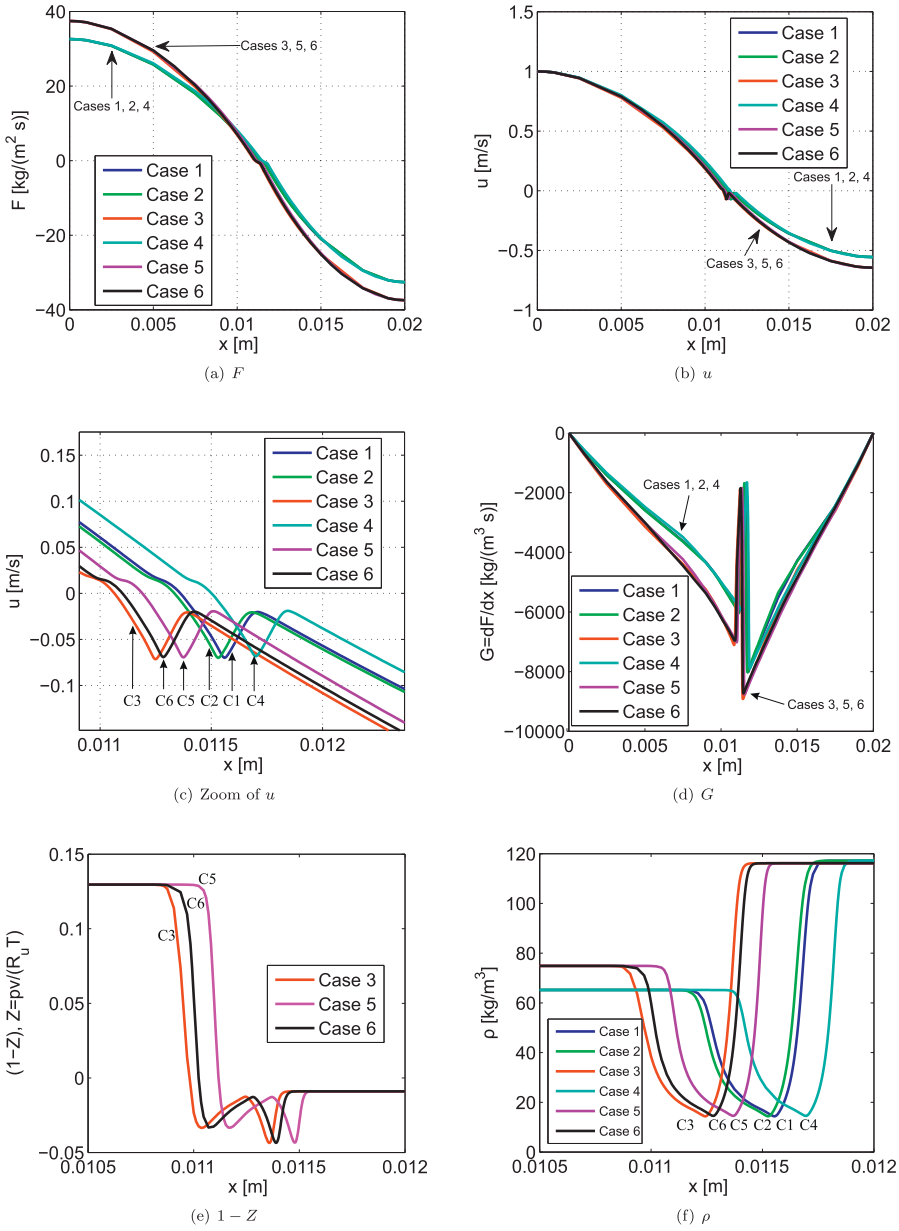

(a) F (b) u (c) Zoom of u (d) G (e) $1 - Z$ (f) ρ

Fig. 6. Comparison of variables among Cases 1 through 6 at 100 atm.

means that more momentum flux comes from the left side of the domain. Hence, the difference on the left boundary of Fig. 6a. Also, an increase of density on the left side combined with almost no change in density on the right side means that the velocity at the exit of the right nozzle must increase in magnitude (again due to the used boundary condition for F, see Eq. (10)). Since the momentum flux equals to ρu^2, the increase in velocity magnitude on the right causes the right momentum flux to rise more than the left flux. The final result is that the stagnation plane in Case 3 gets displaced to the left with respect to Case 1, but it still sits on the right side of the symmetry plane.

Let us turn our attention to the effects caused by the use of the real-gas energy equation (Eq. (5)) instead of the ideal version, together with the enthalpy departure function correction. Figure 7a shows temperature profiles for the different cases. As opposed to the correction in the equation of state, the main effect of mending the energy equation is shifting the flame towards the air nozzle. The flame structure, however, remains almost unaltered, except for a slight decrease in flame temperature for the cases with corrected energy equation, which can be explained if we look at the enthalpy.

Figure 7b portrays the enthalpy departure function and it's percentage difference compared to the sensible enthalpy of the mixture. The correction is more important in the cold regions and in the heating zones. The correction becomes less important in the hot region. Overall, the percentage difference between departure function and sensible enthalpy is below at most 4%. The corrections in enthalpy departure and compressibility factor are very similar among the cases where they apply, with shifts in the x-direction due to the flame location. Their effect diminishes at the location where the flame peaks, confirming the tendency towards ideal-gas behavior in the flame core.

In terms of reactants (Fig. 7c), the different corrections only change the location where the mass fractions drop according to the flame position for each case. Figure 7d shows that the x-coordinate where CO_2 is generated also changes accordingly.

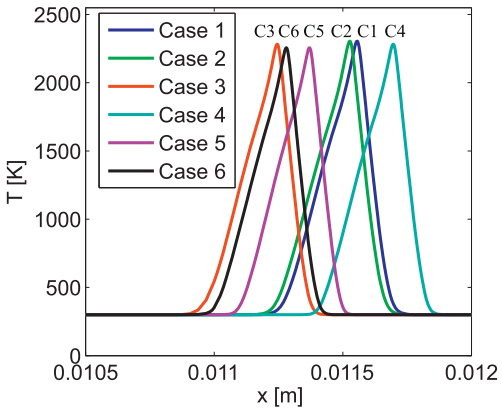

(a) T

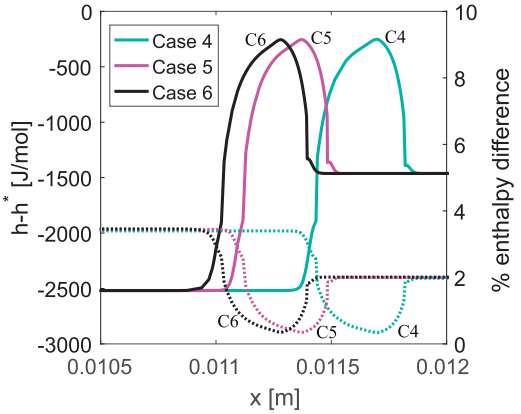

(b) Mixture enthalpy departure and % difference with sensible enthalpy

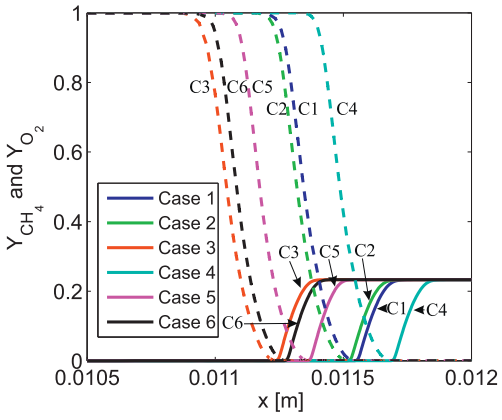

(c) Dashed: Y_{CH_4}, Solid: Y_{O_2}

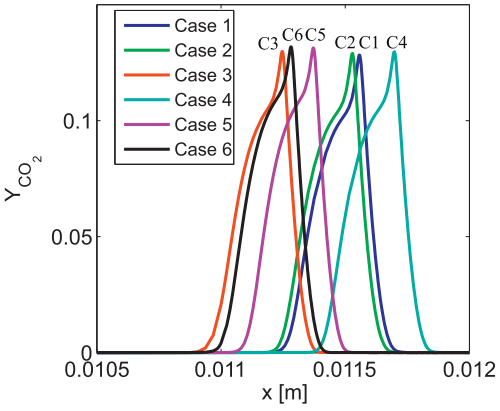

(d) Y_{CO_2}

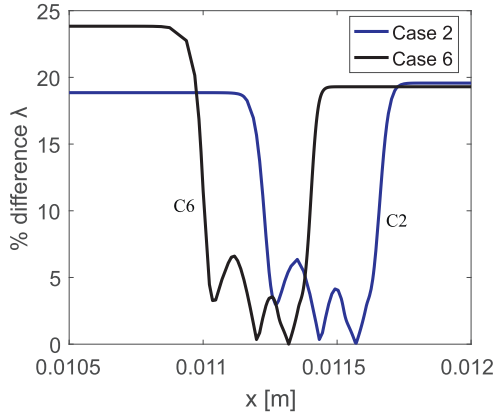

(e) % λ difference between ideal and corrected

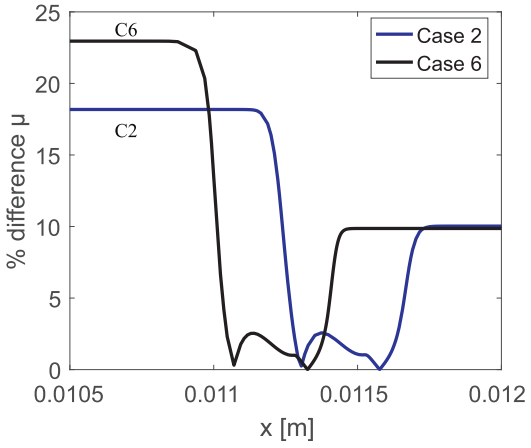

(f) % μ difference between ideal and corrected

Fig. 7. Comparison of variables among Cases 1 through 6 at 100 atm.

Figure 7e and f show the percentage difference between ideal and corrected transport properties for the cases in which they are mended. The difference is about 3% in average in the flame regions, while it becomes 20% or more in the cold regions. The absolute value of transport properties at cold temperatures is much smaller compared to their counterparts at hot temperatures, which brings the percentage difference up even though the absolute difference is not so vast. Thus, great differences with respect to Case 1 were not expected.

6.2. New enthalpy approach: Case 6 vs. Case 7

As discussed in Section 2, our most complete model differs from previous studies because we do not assume $h = \sum_k Y_k h_k$ in the convective term of the energy equation. To assess the consequences of such simplification, enthalpy and temperature profiles are contrasted between the two approaches in this section.

We study the behavior of the mixture enthalpy versus temperature at fixed composition in Fig. 8. The composition is prescribed,

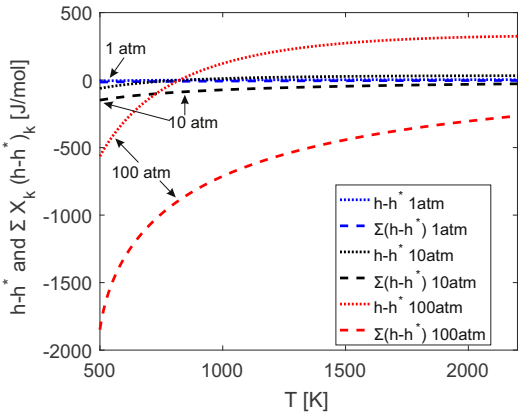

(a) $h - h^*$

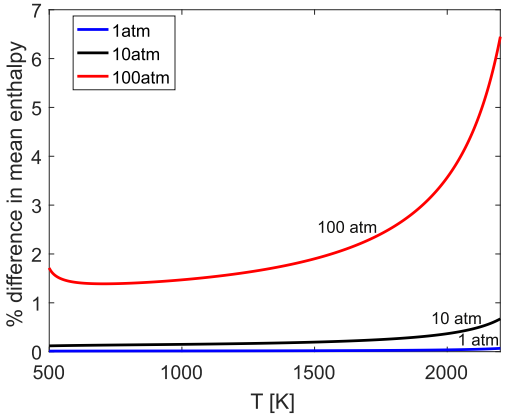

(b) h relative difference between mixture and summation

Fig. 8. Enthalpy curves (with composition fixed at the flame-peak values for Case 7) versus T.

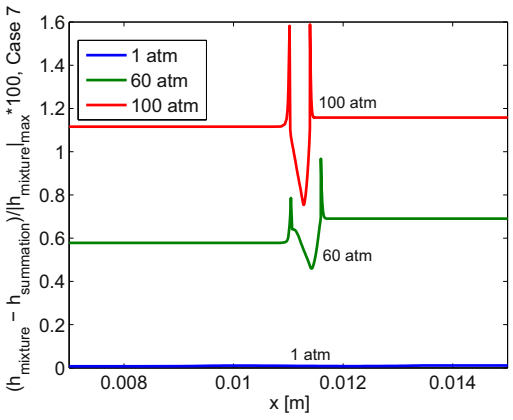

(a) Enthalpy relative difference

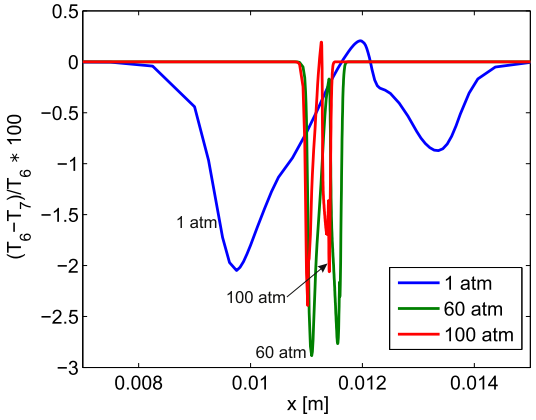

(b) T relative difference between mixture and summation

Fig. 9. Differences in enthalpy and temperature profiles between Case 6 and Case 7.

taken from Case 7 at the x-coordinate where the flame temperature peaks. Figure 8a portrays the enthalpy departure function of the mixture from Eq. (17) (dotted lines) versus the same property but computed from the summation of the individual components times the mass fractions (dashed lines). The departure function is very close to 0 for both cases at atmospheric pressure, consistent with ideal-gas behavior. As pressure is increased, the departure becomes more important. At very high temperature, the departure is closer to zero than at cold temperatures, but it does not behave exactly as in the ideal situation. The enthalpy mixture calculation yields a positive departure above 700 K, while the summation approach always yields negative values. The absolute values of differences between the mixture and the summation approaches are noticeable. Figure 8b shows the percentage difference between the mean enthalpy computed from the mixing rules and the mean enthalpy computed from the summation of components. The differences are bounded above by 1% below 10 atm. They become more important at 100 atm, with differences reaching about 6% relative difference at the highest temperature. With this information, we would like to see what the effect of such differences is on the flame.

If we introduce the composition dependence that exists in the counterflow domain, for example for Case 7, we see in Fig. 9a that the relative difference between computing the enthalpy directly from mixing rules or from the summation approach is below 2%. With this information in mind, we now compare counterflow diffusion flame solutions between Cases 6 and 7 at various pressures. Figure 9b shows temperature percentage differences below 3%, while flame location and structure are practically unaltered.

6.3. Case 6: complete odel

The goal of this section is to analyze Case 6 (which entails our most complete model) in order to obtain conclusions about the pressure effect on the flame and check if the flame structure complies with previously reported correlations with the pressure-weighted strain rate.

Solutions are presented in Fig. 12. Figure 12a shows velocity and temperature profiles. As expected from the momentum-flux ratio, the stagnation plane is to the right of the symmetry point ($x = L/2$). The stagnation plane would lie on the center of the domain if the momentum fluxes ρu^2 at the two nozzles were balanced. However, given the fixed density values of methane and air at the nozzles, the boundary condition $F_{(x=L)}$ (see Eq. (10)) implies that the momentum flux of the methane stream is greater than that of the air stream. Thus, stagnation occurs closer to the air nozzle. See Appendix B for a more detailed comparison between the two boundary conditions. The increase in pressure increases flame temperature and narrows flame width. The first increment in pressure causes the most substantial temperature rise, while further

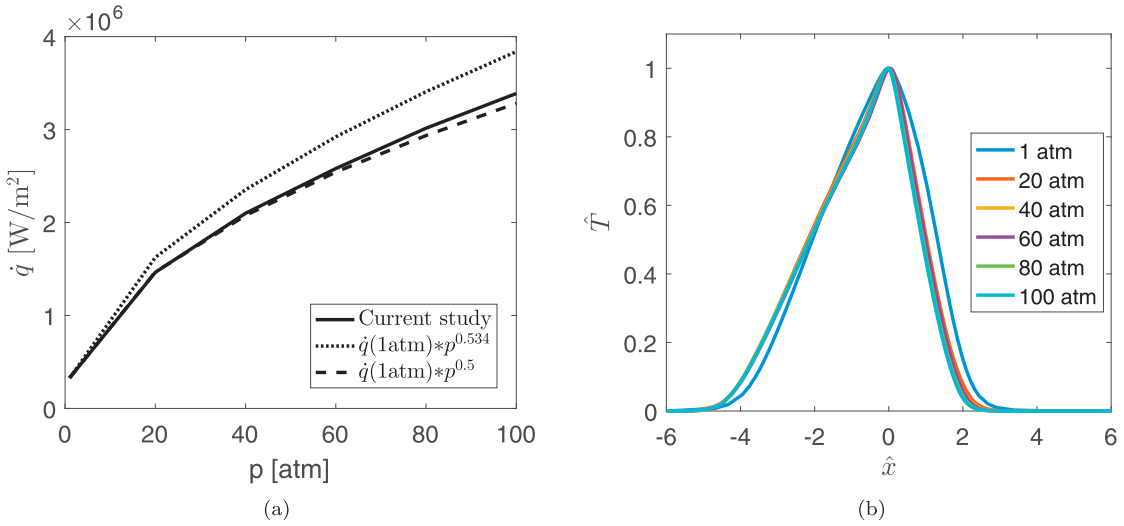

Fig. 10. Heat-release rate and non-dimensional temperature scalings for Case 6 at 100 atm.

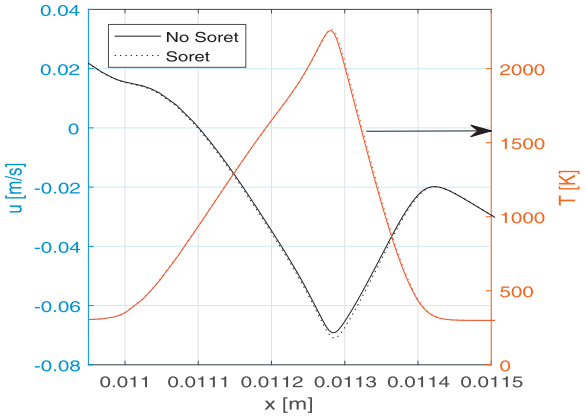

Fig. 11. Soret effect on Case 6 at 100 atm.

escalation in pressure does not imply such a high relative temperature increase. Higher pressure suppresses species dissociation which tends to bring the temperature down, and higher temperature favors dissociation. At higher pressures the kinetics are faster. So, the balance between the pressure and temperature effects on dissociation is determining. However, there is only so much energy that can be extracted from the reaction, so one can not expect a linear flame temperature increase with pressure, but an asymptotic behavior. The flame temperature at 1 atm equals 1987 K, while its value at 100 atm is 2255 K. The x-coordinate where the maximum flame temperature occurs moves closer to the stagnation plane as pressure rises, but it always sits to its right, on the oxidizer side.

Previous publications such as [21] reported correlations between flame temperature and pressure $T_m \sim p^{0.0474}$, and flame thickness with pressure-weighted strain rate $\delta \sim 1/\sqrt{pa}$. a is the strain rate defined as the maximum absolute velocity gradient in the flow field. The flame-thickness scaling obtained in this study was shown in Section 5, Fig. 4, showing close agreement with the $\delta \sim 1/\sqrt{pa}$ correlation. Another correlation for the heat-release rate was obtained in [20]. There, the authors present an analysis using average transport and thermodynamic properties in the flame zone and assume Lewis number of unity, yielding $\dot{q} \sim p^{0.534}\sqrt{a}$. As displayed in Fig. 10a, our result shows that the heat-release rate correlates more accurately with the square root of p.

[47] provides experimental results for laminar counterflow diffusion flames at pressures below 3 MPa. A scaling for the flame temperature is identified, which we repeated in this paper for comparison purposes. The result is shown in Fig. 10, where the normalized temperature and x-coordinate are $\hat{T} = (T - T_o)/(T_{MAX} - T_o)$ and $\hat{x} = x/\delta_{diff}$, respectively. $\delta_{diff} = \sqrt{\frac{\alpha_o}{a}\frac{p_o}{p}}$, where α_o is a thermal diffusivity evaluated at a mean temperature of 1000 K and at 1 atm for the oxidizer stream, and a is the strain rate. As the plot highlights, the curves at different pressures collapse to a single curve, as suggested in the provided reference. The curve at the highest pressure (100 atm) shows the greater departure, suggesting that this correlation might only be valid up to a certain pressure threshold. Real-gas transport properties might explain the departure at high pressures.

As anticipated in Section 5, a check has been performed on the effect of including the thermophoretic contribution to the diffusion velocity. At very high pressures, the flame thickness is very narrow and the temperature gradient is at its highest magnitude. Hence, one could argue that the Soret effect may play an important role. On the contrary, the result displayed in Fig. 11 shows that the differences between including and neglecting the Soret effect are very small. Inclusion of this effect tends to increase the flame temperature slightly. The local velocity peak in the reaction zone also increases modestly.

Figure 12c shows the mass fractions of methane and oxygen. The curves become much steeper at high pressures due to the smaller flame thickness. The following may be difficult to see by eye inspection and observations; they were made with a closer computational view. At 1 atm, there is coexistence of both reactants near the region of maximum temperature, although mass fraction values are small (i.e., < 0.005). Methane that diffuses into the oxygen decays quickly, while oxygen diffuses a much longer distance into the methane side and past the stagnation plane. In contrast, at 100 almost no overlapping exists. For example, at $x = 11.54$ mm, the mass fraction of both reactants is < 0.0005 and it decays very quickly moving in either direction. Figure 12d represents carbon dioxide mass fractions. This combustion product is generated along a broader region at low pressure, and its presence narrows as pressure raises. CO_2 mass fraction peak value also increases with pressure. Similarly to the flame temperature

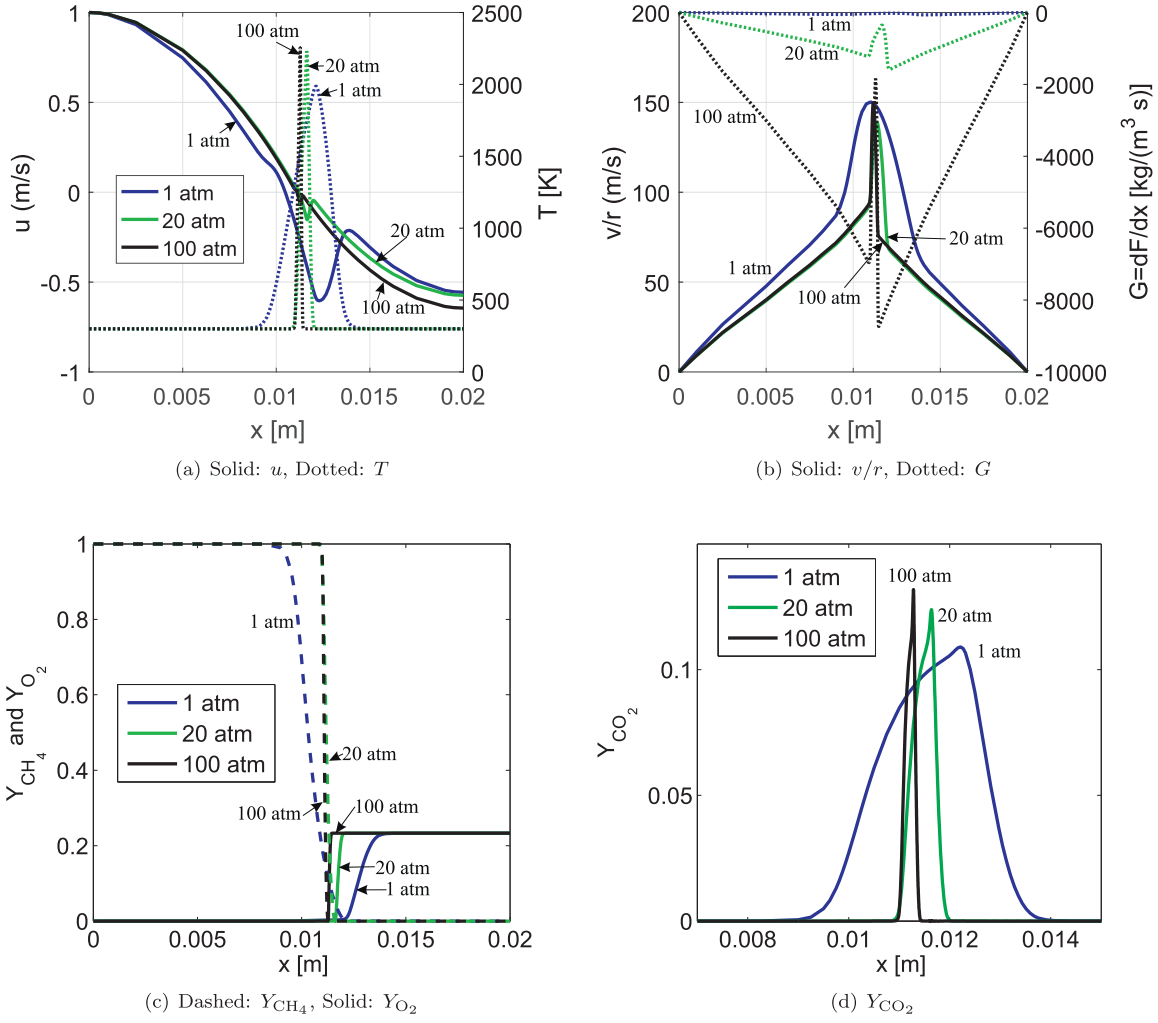

(a) Solid: u, Dotted: T

(b) Solid: v/r, Dotted: G

(c) Dashed: $Y_{\mathrm{CH_4}}$, Solid: $Y_{\mathrm{O_2}}$

(d) $Y_{\mathrm{CO_2}}$

Fig. 12. Set of variables for Case 6 at various pressures.

behavior, the most substantial increment in CO_2 mass fraction occurs when pressure is raised from 1 to 20 atm. In comparison, further increments do not seem to yield such a strong effect. The reasoning behind this is the same as for the temperature profiles.

6.4. Case 8: methane and water vapor

Consider now Case 8, in which water vapor flows into the domain premixed with the methane. Three sub-cases are studied with increasing amounts of water vapor: 10, 20 and 40%. For brevity, only a few representative plots are reported for the last case in Fig. 13. The trends with increasing water content are discussed below.

At 10% water vapor, temperature profiles highlight that raising pressure yields identical effects as for previous cases: it increases flame temperature, it narrows flame width, and the temperature peak moves closer to the stagnation plane. Flame temperature at 1 atm is 2029 K while it equals 2305 K at 100 atm. These values are 42 K and 49 K hotter than for Case 6, respectively. Note that the temperature boundary condition on the left side has been increased by 300 K with respect to all the previous cases. Thus, a new simulation of Case 6 where the left temperature boundary condition matches the 600 K of Case 8a is performed. The resulting flame temperature at 1 atm is 2043 K. Now, Case 8a at 1 atm is 14 K colder compared to this new result. Therefore, addition of 10% of water acts as an energy sink. Nevertheless, 14 K is not a very substantial temperature difference. For enthalpy departure, the cold region of the air stream is unchanged with respect to Case 6. The curves on the cold region of the fuel stream, however, are closer to each other, highlighting more sensitivity to the temperature boundary condition increment than to pressure.

Density is generally lower on the fuel side compared to Case 6. The presence of water, which is heavier than methane, tends to increase the density. However, having a higher temperature on the left boundary is a dominant effect. Regarding the compressibility factor, the trend is inverted on the fuel side with respect to Case 6. Here $(1-Z)$ is becoming more negative with increasing pressure, which also contributes to reduce the density.

Water product is generated in the flame region, where its mass fraction becomes greater than at the boundary for all pressures. The peak value increases with pressure. The previous trends on CO_2 production do not seem to be altered with the presence of extra water. The hotter gas coming from the left enhances both μ and λ on the fuel side, comparing with Case 6. The properties are not altered in the rest of the domain.

The water content in the fuel mixture is elevated to 20% in Case 8b. The flame temperature is 21 K colder at 1 atm and 31 K colder at 100 atm compared to Case 8a. These flame temperatures are also lower than the case with no water. Again, the energy sink effect of water is dominant, and the consequence is even lower

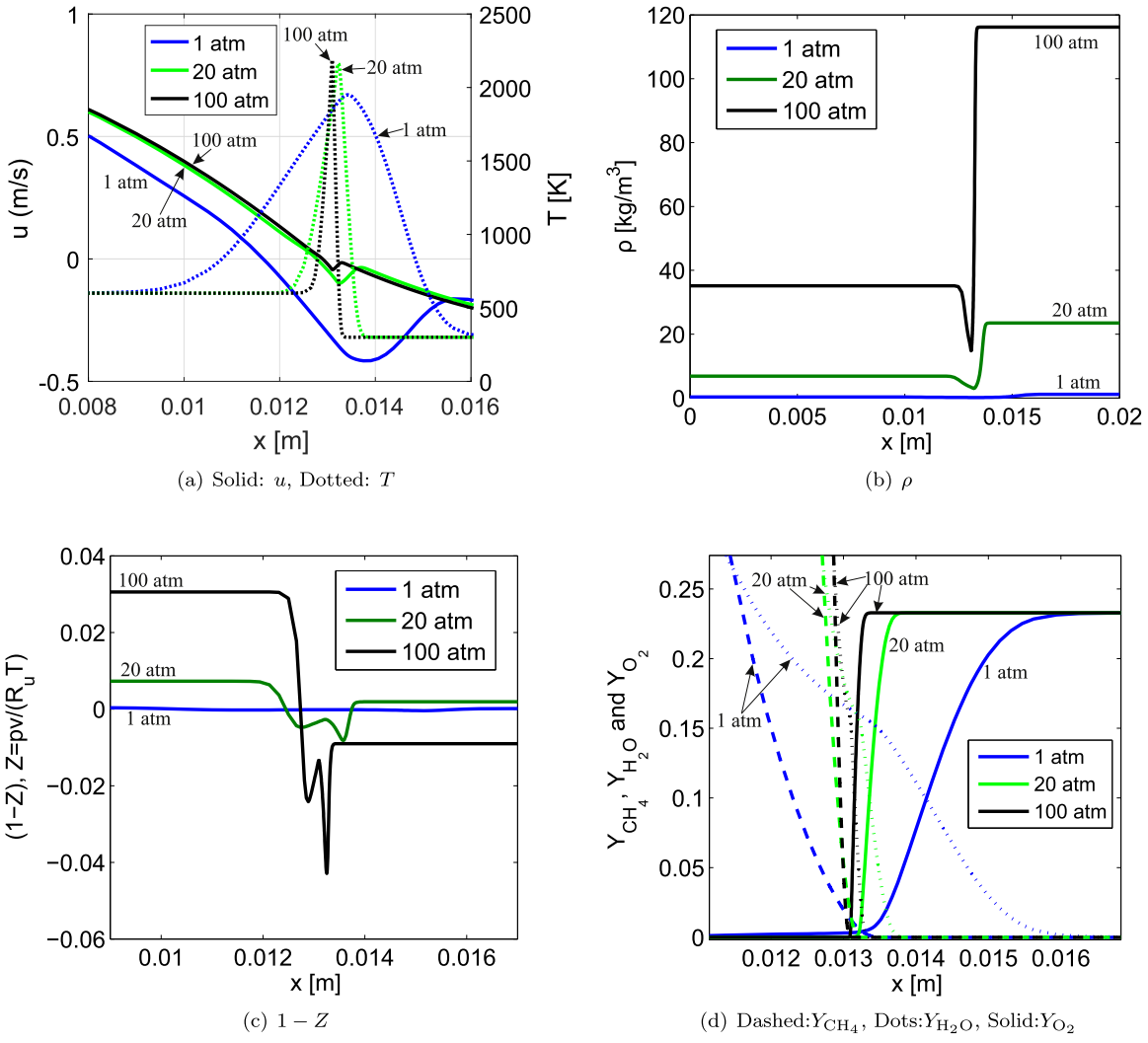

(a) Solid: u, Dotted: T

(b) ρ

(c) $1 - Z$

(d) Dashed:Y_{CH_4}, Dots:Y_{H_2O}, Solid:Y_{O_2}

Fig. 13. Set of variables for Case 8c with 40% water vapor in the fuel stream.

flame temperatures when more water is added. Density remains practically unaltered with respect to Case 8a. The presence of more water content on the left side of the domain affects the compressibility factor where all the $1 - Z$ curves are moved in the positive direction, tending to increase the density of the mixture. Comparison against Case 8a indicates that the presence of extra water on the left stream increases the magnitude of the enthalpy departure function keeping the same sign in the cold zone on the fuel side. In the heat-release zone, the enthalpy departure behaves as in Case 8a.

Mass fraction of water features a local peak in the flame region, where more water is generated as a combustion product, but its magnitude now is lower than the 0.2 value coming from the left boundary. No changes occur in the CO_2 mass fraction. Transport properties are also not altered.

Figure 13 contains the solutions for Case 8c in which the water content in the fuel stream is 40%. Similarly to all previous cases, the stagnation plane lies to the right of the symmetry plane. Peak temperature at 1 atm is 56 K colder comparing with Case 8b, and it is 90 K colder at 100 atm. Density is shown in Fig. 13b, portraying a slight increase with respect to Case 8b on the cold fuel stream region. The $1 - Z$ trend discussed for Case 8b is even more obvious here as shown in Fig. 13c, where all the curves are now positive at the left boundary.

Methane, oxygen, and water mass fractions are represented in Fig. 13d. The water mass fraction flowing from the left is now too high compared to the water generated as a combustion product. This translates into a smooth decrease of the mass fraction gradient in the flame zone, which becomes steep again for greater x. The local peak that was identified in Cases 8a and 8b no longer exists. The enthalpy departure function becomes more significant along the cold region of the fuel side, while it is diminished within the flame zone. Transport properties remain unaffected.

The water content in the fuel stream has been increased above 40% with the goal of finding the burning limit. The greatest percentage of H_2O resulting in a flame solution is of 67% at 1 atm, with a flame temperature of 1607 K. Further study of this limit is required, including results at high pressure.

7. Conclusion

Analysis of combustion at high pressure with the presence of dense fluids requires relaxation of certain assumptions that are commonly taken. The use of ideal-gas approximations in these scenarios requires justification. This computational study presents solutions for a steady laminar counterflow diffusion flame using a real-gas model. The relative effect of different relaxations is analyzed by solving a one-dimensional system of differential

equations equipped with detailed chemistry and detailed transport. The considered reactants are methane and air. A path for error estimates is identified in this canonical configuration. It can serve as a template for other researchers. In particular, three different corrections have been examined: (I) replacement of the ideal-gas law by a suitable non-ideal cubic equation of state; (II) consideration of the energy equation for real gases equipped with properly corrected thermodynamic properties such as enthalpy; (III) modification of transport properties such as dynamic viscosity and thermal conductivity. Solutions are presented for several cases in which each of the corrections are applied individually or combined. Results show that the largest correction is the replacement of the ideal-gas law, followed by the amendment of the energy equation, while rectification of transport properties is less significant. Substantial differences appear mainly in terms of flame location. Correction of the equation of state moves the flame towards the stagnation plane, closer to the fuel stream, whereas the correction of the energy equation has the opposite effect. The main differences in flame location are due to the fact that the real-gas equation of state provides more accurate values of the flow properties in the cold regions. This conclusion should be kept in mind during the design process of high-pressure combustors.

Even with the new corrections, heat-release rate, flame temperature, and thickness still follow well previously published correlations with pressure and pressure-weighed strain rate, respectively. Radiative heat losses and the Soret effect are shown to be negligible, even at the highest pressure.

An analysis has been developed on the existence of turbulence. Specifically, four plausible causes of turbulence in the counterflow have been identified, and based on established practice, we demonstrated that the first three mechanisms can essentially be eliminated. We showed, using an extremely conservative analysis (i.e., with elimination of turbulent kinetic energy diffusion and dissipation and with maximizing of the production term), that the fourth mechanism will not generate any significant turbulence for the applicable length scale.

The presented form of the energy equation is more general compared to the version commonly found in the literature, which assumes in the convective term that $h = \sum_k Y_k h_k$. Comparison of the two shows discrepancies in terms of flame temperature and enthalpy that are below 3%.

The difference between matching mass fluxes versus momentum fluxes between the two nozzles affects only the flame location and does not does not impact any of our major findings.

Furthermore, computations are made for a case equipped with the most complete model and including water vapor premixed with the methane. Solutions are presented for percentages of water vapor equal to 10, 20 and 40% by mass. Presence of water not being generated as a combustion product acts as an energy sink; therefore flame temperatures decrease with increasing water content. Escalation of pressure produces similar effects on the flame for the problem with extra water and without it. These effects include increase of flame temperature, narrowing the flame region, and displacement of the flame position closer to the stagnation plane. This plane is located to the right of the symmetry line, closer to the air nozzle, for all the studied cases. The greatest percentage of premixed water content at which a flame solution has been obtained equals 67% at 1 atm. This limit requires further exploration, specially at higher pressures.

Commercial software packages use chemical kinetic laws established for lower pressure range. Chemical equilibrium laws at very high pressure require the use of fugacity rather than partial pressure. Comparative calculations have been presented for a range of prescribed temperatures and at 100 atm. Results indicate differences below 1%. Thus, application of these kinetic laws at the higher pressures with regard to the ability to predict accurately equilibrium and rates becomes more comfortable. However, chemical pathways may still be different at high pressures.

Acknowledgments

This research was supported by the NSF under Grant CBET-1333605. The first author appreciates the Balsells Fellowship support.

Appendix A. Chemical equilibrium

Reaction mechanisms provide data to compute the forward rates of each reaction that is part of the mechanism. Reverse rates are usually computed from forward rates and the principle of chemical equilibrium. This principle is embedded in most commercial codes, usually based on the classical partial pressures. At high pressure, however, fugacities should be used instead of partial pressures for better accuracy in chemical-equilibrium calculation. The theory for chemical kinetics of non-ideal gases is not well established. So, we are forced to use the same kinetics developed for ideal gases. The goal of this section is to assess the differences that arise when we calculate the product species composition in equilibrium of a hydrocarbon reaction, both using the classical ideal formulation and the non-ideal counterpart.

In the following, the index i corresponds to a particular reaction while the index k indicates species. ν_{ki} represents the stoichiometric coefficient of species k in the reaction i. $X^{classic}$ and X are the mole fractions of the product species in chemical equilibrium for the classical case and for the non-ideal case, respectively.

The equilibrium constant is determined from thermodynamics:

$$K_{p_i}(T) = exp(-\frac{\Delta G_i^o}{R_u T}) = exp(\frac{\Delta S_i^o}{R_u} - \frac{\Delta H_i^o}{R_u T}), \tag{A.1}$$

where ΔG_i^o, ΔH_i^o, and ΔS_i^o are the Gibbs function, enthalpy, and entropy changes that occur in passing completely from reactants to products in the ith reaction.

Table A.2
$X_k^{classic}/X_k$, stoichiometric: $\Phi = 1.0$.

T(K)	O_2	CO_2	H_2O	CO	OH	H	H_2	O	N	N_2	NO
2300	1.00569	0.99992	0.99995	1.00267	1.00164	1.00013	1.00660	1.00291	1.00236	0.99999	1.00037
2400	1.00523	0.99988	0.99994	1.00260	1.00141	1.00012	1.00626	1.00268	1.00227	0.99998	1.00024
2500	1.00484	0.99984	0.99992	1.00251	1.00122	1.00010	1.00594	1.00248	1.00219	0.99997	1.00014
2600	1.00452	0.99978	0.99989	1.00242	1.00109	1.00011	1.00570	1.00232	1.00212	0.99997	1.00007
2700	1.00434	0.99970	0.99985	1.00236	1.00123	1.00028	1.00580	1.00230	1.00207	0.99996	1.00005
2800	1.00417	0.99961	0.99980	1.00229	1.00134	1.00043	1.00585	1.00229	1.00204	0.99994	1.00002
2900	1.00401	0.99950	0.99975	1.00220	1.00141	1.00056	1.00587	1.00227	1.00200	0.99993	1.00000
3000	1.00384	0.99937	0.99968	1.00209	1.00145	1.00066	1.00585	1.00224	1.00198	0.99991	0.99997

Table A.3
$X_k^{classic}/X_k$, fuel-lean: $\Phi = 0.8$.

T(K)	O_2	CO_2	H_2O	CO	OH	H	H_2	O	N	N_2	NO
2300	1.00022	0.99997	0.99999	1.00556	1.00050	1.00168	1.00974	1.00023	1.00240	1.00003	0.99766
2400	1.00024	0.99995	0.99998	1.00528	1.00042	1.00158	1.00921	1.00024	1.00232	1.00003	0.99777
2500	1.00027	0.99992	0.99997	1.00501	1.00035	1.00148	1.00871	1.00026	1.00224	1.00002	0.99788
2600	1.00031	0.99988	0.99995	1.00475	1.00032	1.00141	1.00831	1.00029	1.00217	1.00002	0.99798
2700	1.00037	0.99982	0.99993	1.00458	1.00050	1.00151	1.00825	1.00039	1.00213	1.00001	0.99808
2800	1.00045	0.99973	0.99989	1.00438	1.00065	1.00159	1.00815	1.00049	1.00210	1.00000	0.99819
2900	1.00055	0.99962	0.99984	1.00415	1.00077	1.00164	1.00801	1.00060	1.00207	0.99998	0.99829
3000	1.00065	0.99948	0.99978	1.00389	1.00087	1.00167	1.00783	1.00071	1.00204	0.99996	0.99840

Table A.4
$X_k^{classic}/X_k$, fuel-rich: $\Phi = 1.1$.

T(K)	O_2	CO_2	H_2O	CO	OH	H	H_2	O	N	N_2	NO
2300	1.01385	1.00034	0.99986	0.99900	1.00353	0.99799	1.00230	1.00695	1.00236	1.00000	1.00443
2400	1.01298	1.00030	0.99987	0.99913	1.00321	0.99809	1.00218	1.00651	1.00228	1.00000	1.00410
2500	1.01216	1.00026	0.99987	0.99926	1.00291	0.99819	1.00209	1.00610	1.00220	0.99999	1.00379
2600	1.01139	1.00021	0.99987	0.99939	1.00268	0.99831	1.00208	1.00572	1.00212	0.99999	1.00350
2700	1.01092	1.00017	0.99984	0.99951	1.00275	0.99855	1.00233	1.00555	1.00207	0.99998	1.00333
2800	1.01024	1.00009	0.99980	0.99970	1.00273	0.99883	1.00264	1.00527	1.00203	0.99997	1.00306
2900	1.00937	0.99997	0.99974	0.99994	1.00264	0.99913	1.00301	1.00491	1.00200	0.99995	1.00268
3000	1.00841	0.99981	0.99967	1.00020	1.00249	0.99943	1.00340	1.00449	1.00197	0.99993	1.00225

In the classical case, the equilibrium constant for a mixture of ideal gases is based on partial pressures:

$$K_{p_i} = \frac{\prod_k (P_k/P^o)^{\nu_{ki}^{products}}}{\prod_k (P_k/P^o)^{\nu_{ki}^{reactants}}} = \frac{\prod_k (X_k^{classical})^{\nu_{ki}^{products}}}{\prod_k (X_k^{classical})^{\nu_{ki}^{reactants}}} \left(\frac{P}{P^o}\right)^{\Delta\nu_i}, \tag{A.2}$$

where P^o is the standard state pressure of 1 atm, and $\Delta\nu_i = \sum_k \nu_{ki}^{products} - \sum_k \nu_{ki}^{reactants}$.

For non-ideal systems, fugacities must be employed [48]:

$$K_{p_i} = \frac{\prod_k (f_k/P^o)^{\nu_{ki}^{products}}}{\prod_k (f_k/P^o)^{\nu_{ki}^{reactants}}} = \frac{\prod_k (\phi_k X_k)^{\nu_{ki}^{products}}}{\prod_k (\phi_k X_k)^{\nu_{ki}^{reactants}}} \left(\frac{P}{P^o}\right)^{\Delta\nu_i}, \tag{A.3}$$

where f_k is the fugacity of species k and $\phi_k = f_k/(X_k P)$ is the fugacity coefficient. These expressions for both classical and non-ideal cases will be used in the laws of mass action below.

A generic reaction between a hydrocarbon and air is

$$\begin{aligned} & n_F\left[C_nH_m + \frac{n+m/4}{\Phi}(rmO_2 + 3.76N_2)\right] \\ & \rightarrow X_1O_2 + X_2CO_2 + X_3H_2O + X_4CO + X_5OH \\ & + X_6H + X_7H_2 + X_8O + X_9N + X_{10}N_2 + X_{11}NO, \end{aligned} \tag{A.4}$$

where n_F is the number of moles that gives one mole of products, X_1 through X_{11} are the mole fractions of the considered product species, and Φ is the fuel-to-air equivalence ratio.

To determine the mass fractions X_k ($k = 1, ..., 11$) and n_F at equilibrium, we use four mass balance equations, seven laws of mass action associated with elementary reactions, and the fact that the summation of all mass fractions must equal one. In the following, $r = \frac{n+m/4}{\Phi}$.

$$\begin{cases} n\ n_F = X_2 + X_4 \\ m\ n_F = 2X_3 + X_5 + X_6 + 2X_7 \\ 2\ r\ n_F = 2X_1 + 2X_2 + X_3 + X_4 + X_5 + X_8 + X_{11} \\ 7.52\ r\ n_F = X_9 + 2X_{10} + X_{11}. \end{cases} \tag{A.5}$$

The elementary reactions and their corresponding laws of mass action (based on partial pressures) are

$$\begin{cases} 1/2O_2 \leftrightarrows O, & K_{p_1} = \frac{X_8}{X_1^{1/2}}\left(\frac{P}{P_o}\right)^{1/2} \\ 1/2H2 \leftrightarrows H, & K_{p_2} = \frac{X_6}{X_7^{1/2}}\left(\frac{P}{P_o}\right)^{1/2} \\ 1/2N_2 \leftrightarrows N, & K_{p_3} = \frac{X_9}{X_{10}^{1/2}}\left(\frac{P}{P_o}\right)^{1/2} \\ 1/2O2 + 1/2N2 \leftrightarrows NO, & K_{p_4} = \frac{X_{11}}{X_1^{1/2}X_{10}^{1/2}} \\ CO + 1/2O_2 \leftrightarrows CO_2, & K_{p_5} = \frac{X_2}{X_4X_1^{1/2}}\left(\frac{P}{P_o}\right)^{-1/2} \\ H_2 + 1/2O_2 \leftrightarrows H_2O, & K_{p_6} = \frac{X_3}{X_7X_1^{1/2}}\left(\frac{P}{P_o}\right)^{-1/2} \\ 1/2H_2 + 1/2O_2 \leftrightarrows OH, & K_{p_7} = \frac{X_5}{X_7^{1/2}X_1^{1/2}}. \end{cases} \tag{A.6}$$

These laws of mass action are readily modified for the non-ideal case by multiplying each mass fraction by its fugacity coefficient, according to Eq. (A.3). The fugacity coefficients are obtained according to our choice of EoS, from the following expression [38]:

$$ln(\phi_k) = \frac{b_k}{b}(Z-1) - ln(Z-B) - \frac{A}{B}\left(2\frac{a_k^{0.5}}{a^{0.5}} - \frac{b_k}{b}\right) ln\left(1 + \frac{B}{Z}\right). \tag{A.7}$$

Eqs. (A.5) and (A.6), together with $\sum_{k=1}^{11} X_k = 1$, form a system of non-linear algebraic equations. We use the Matlab solver "fsolve", together with the "trust-region-dogleg" algorithm. The pressure is prescribed at 100 atm, and the temperature is varied from 2300 to 3000 K. The product composition is obtained for three different equivalence ratios ($\Phi = 1$, 0.8, and 1.1). Ratios between the mole fractions for the classical case and those for the non-ideal case are formed and presented in Tables A.2–A.4.

We can see from the results that the differences are very small, always below 1% for the stoichiometric and fuel-lean cases. Only the fuel-rich case shows ratios slightly above 1%, but it only exceeds this value by a few decimals. These results make the use of the classical chemical equilibrium more comfortable at elevated pressures for combustion problems. However, one must keep in mind that differences in chemical pathways may still exist, and therefore the uncertainty on reaction rates also remains.

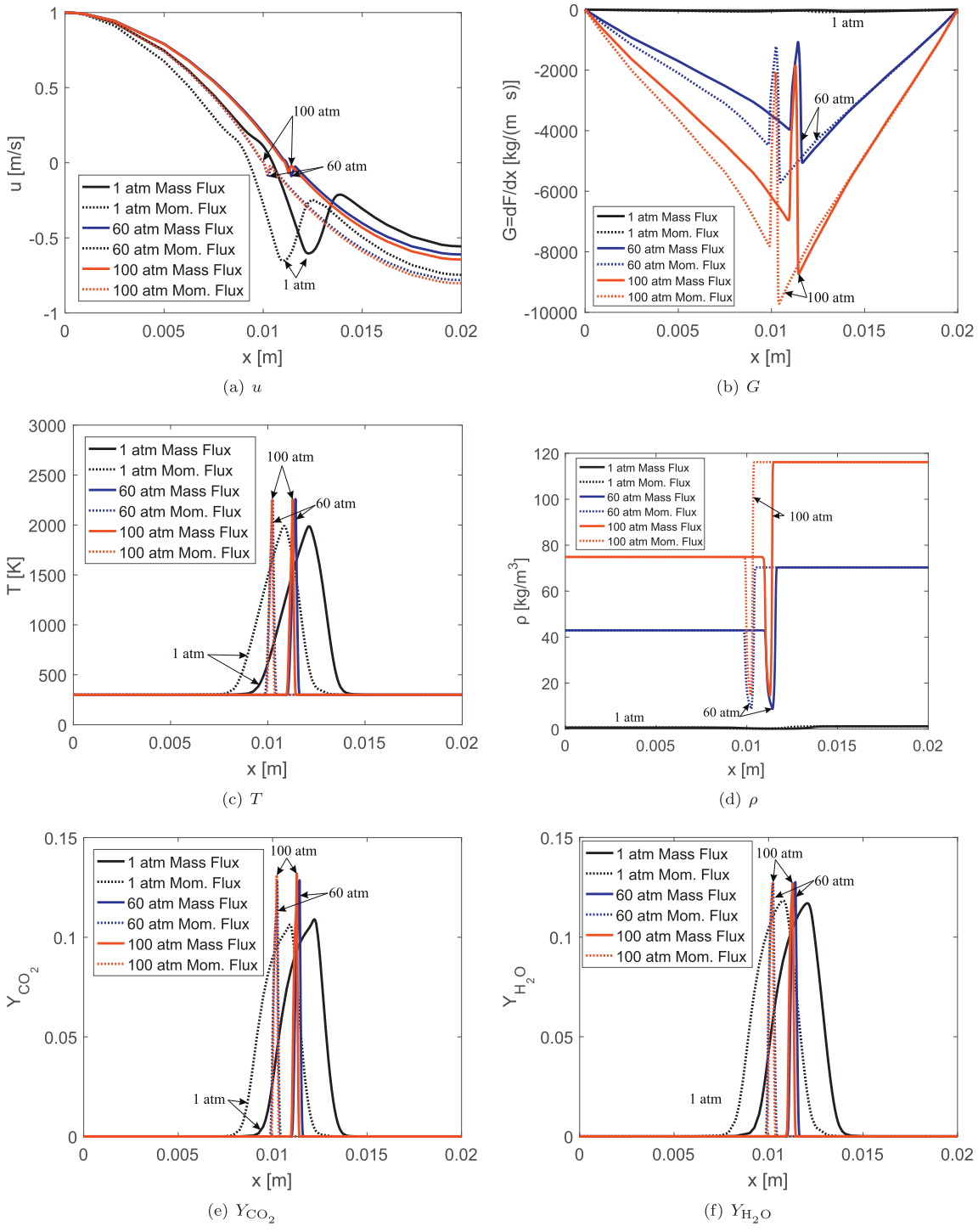

(a) u (b) G (c) T (d) ρ (e) Y_{CO_2} (f) Y_{H_2O}

Fig. B.14. Comparison between matching mass fluxes versus matching momentum fluxes for Case 6.

Appendix B. Mass flux vs momentum flux

The differences between the boundary conditions for F introduced by Eq. (10) (matching the mass fluxes of both nozzles), versus matching the momentum fluxes are highlighted in Fig. B.14. It includes velocity, temperature, density, and mass fraction curves for Case 6 at various pressures. We observe that the main difference between the two boundary conditions is a shift in the x-coordinate of the flame and the stagnation plane. Finding the stagnation plane in the center of the domain is expected when balancing the momentum fluxes. This clearly occurs at elevated pressures. At atmospheric pressure, however, the heat release zone is wide enough to perturb the velocity field and cause stagnation to occur closer to the fuel side.

References

[1] J. Foster, R.S. Miller, Fundamentals of high pressure combustion, in: M. Lackner (Ed.), High Pressure Processes In Chemical Engineering, ProcessEng Engineering, 2010, pp. 53–75.
[2] T. Kamimoto, H. Kobayashi, Combustion processes in diesel engines, Prog. Eng. Comb. Sci. 17 (1991) 163–189.
[3] R.D. Reitz, C.J. Rutland, Development and testing of diesel engine CFD models, Prog. Eng. Comb. Sci. 21 (1995) 173–196.

[4] R. Marcer, P.L. Cottier, H. Chaves, B. Argueyrolles, C. Habchi, B. Barbey, A validated numerical simulation of diesel injector flow using a VOF method, Technical Report, SAE International (Society of Automotive Engineers), 2000.
[5] G.M. Bianchi, P. Pelloni, F.E. Corcione, L. Allocca, F. Luppino, Modeling atomization of high-pressure diesel sprays, J. Eng. Gas Turb. Power 123 (2001) 419–427.
[6] E. de Villiers, A.D. Gosman, H.G. Weller, Large eddy simulation of primary diesel spray atomization, Technical Report, SAE International (Society of Automotive Engineers), 2004.
[7] J.P. Delplanque, W.A. Sirignano, Numerical study of the transient vaporization of an oxygen droplet at sub- and super-critical conditions, Int. J. Heat Mass Transf. 36 (2) (1993) 303–314.
[8] W. Mayer, H. Tamura, Propellant injection in a liquid oxygen/gaseous hydrogen rocket engine, J. Propul. Power 12 (1996) 1137–1147.
[9] J.P. Delplanque, W.A. Sirignano, Transcritical liquid oxygen droplet vaporization: effect on rocket combustion instability, J. Propul. Power 12 (2) (1996) 349–357.
[10] L. Pons, N. Darabiha, S. Candel, G. Ribert, V. Yang, Mass transfer and combustion in transcritical non-premixed counterflows, Combust. Theor. Model. 13 (2009) 57–81.
[11] E.D. Sloan, C.A. Koh, Clathrate hydrates of natural gases, 3rd ed., CRC Press Taylor and Francis, 2007.
[12] K.A. Kvenvolden, Methane hydrate - a major reservoir of carbon in the shallow geosphere? Chem. Geol. 71 (1988) 41–51.
[13] T. Bar-Kohany, W.A. Sirignano, Transient combustion of a methane-hydrate sphere, Combust. Flame (2015).
[14] C.K. Law, Combustion physics, Cambridge University Press, Cambridge, UK, 2006.
[15] F.A. Williams, Combustion theory, 2nd ed., The Benjamin/Cummings Publishing Company, Inc., Menlo Park, CA, 1985.
[16] S.R. Turns, An introduction to combustion: concepts and applications, 3rd ed., McGraw Hill, 2011.
[17] F.E. Marble, J.E. Broadwell, The coherent flame model for turbulent chemical reactions, Technical Report, Project SQUID, Report TRW-9-PU, 1977.
[18] G. Ribert, N. Zong, V. Yang, L. Pons, N. Darabiha, S. Candel, Counterflow diffusion flames of general fluids: oxygen/hydrogen mixtures, Combust. Flame 154 (2008) 319–330.
[19] G. Lacaze, J.C. Oefelein, A non-premixed combustion model based on flame structure analysis at supercritical pressures, Combust. Flame 159 (2012) 2087–2103.
[20] H. Huo, X. Wang, V. Yang, A general study of counterflow diffusion flames at subcritical and supercritical conditions: oxygen/hydrogen mixtures, Combust. Flame 161 (2014) 3040–3050.
[21] X. Wang, H. Huo, V. Yang, Counterflow diffusion flames of oxygen and n-alkane hydrocarbons ($CH_4 - C_{16}H_{34}$) at subcritical and supercritical conditions, Combust. Sci. Technol. 187 (2015) 60–82.
[22] G. Amantini, J.H. Frank, M.D. Smooke, A. Gomez, Computational and experimental study of steady axisymmetric non-premixed methane counterflow flames, Combust. Theor. Model. 11 (2007) 47–72.
[23] U. Niemann, K. Seshadri, F.A. Williams, Methane, ethane, and ethylene laminar counterflow diffusion flames at elevated pressures: experimental and computational investigations up to 2.0 MPa, Combust. Flame 161 (2014) 138–146.
[24] L. Piller, M. Idir, J. Molet, A. Matynia, S. de Persis, Experimental study and modelling of Nox formation in high pressure counter-flow premixed CH_4/air flames, Fuel 150 (2015) 394–407.
[25] L. Figura, F. Carbone, A. Gomez, Challenges and artifacts of probing high–pressure counterflow laminar diffusion flames, Proc. Combust. Inst. 35 (2015) 1871–1878.
[26] A. Abbud-Madrid, E.P. Riedel, J.T. McKinnon, The Influence of Water Mists on Premixed Flame Propagation in Microgravity, in: O. Minster, B. Schürmann (Eds.), Proceedings of the First International Symposium held 10-15 September, 2000 in Sorrento, Italy on Microgravity Research and Aplications in Physical Sciences and Biotechnology, European Space Agency, ESA SP-454 (2001), pp. 313–320.
[27] V. Ricchiuti, R.E. Padilla, S.Karnani, D. Dunn-Rankin, Cantera simulations of water-laden methane/air nonpremixed counterflow flames, 8th US National Combustion Meeting (2013).
[28] V. Giovangigli, L. Matuszewski, Numerical simulation of transcritical strained laminar flames, Combust. Flame 159 (2012) 2829–2840.
[29] M.I. Hassan, A.T. Brimmo, Modeling in-cylinder water injection in a 2-stroke internal combustion engine, Energy Proced. 75 (2015) 2331–2336.
[30] A. Yoshida, R. Takasaki, K. Kashiwa, H. Naitob, Y. Saso, Extinguishment of counterflow methane/air diffusion flame by polydisperse fine water droplets, Combust. Flame 160 (2013) 1357–1363.
[31] J.P. Wilson, Effects of water injection and increased compression ratio in a gasoline spark ignition engine, University of Idaho, Idaho, 2011 Ph.D. thesis.
[32] D. Liu, A.M. Zghoul, Z. Li, B. Tan, K.L. Lockwood, R.H. Essenhigh, High intensity combustion of coal with water injection, Combust. Flame 63 (1986) 49–57.
[33] M.D. Smooke, I.K. Puri, K. Seshadri, A comparison between numerical calculations and experimental measurments of the structure of a counterflow diffusion flame burning diluted methane in diluted air, Symp. (Int.) Combust. (1986) 1783–1792.
[34] R.J. Kee, J.A. Miller, G.H. Evans, A computational model of the structure and extinction of strained, opposed flow, premixed methane-air flames, Symp. (Int.) Combust. (1988) 1479–1494.
[35] T. Chung, M. Ajlan, L.L. Lee, K.E. Starling, Generalized multiparameter correlation for nonpolar and polar fluid transport properties, Ind. Eng. Chem. Res. 27 (1988) 671–679.
[36] U. Niemann, K. Seshadri, F.A. Williams, Accuracies of laminar counterflow flame experiments, Combust. Flame 162 (2015) 1540–1549.
[37] G.P. Smith, D.M. Golden, M. Frenklach, N.W. Moriarty, B. Eiteneer, M. Goldenberg, C.T. Bowman, R.K. Hanson, S. Song, W.C.G. Jr., V.V. Lissianski, Z. Qin, Grimech 3.0, 2000, http://www.me.berkeley.edu/gri_mech/.
[38] G. Soave, Equilibrium constants from a modified Redlich–Kwong equation of state, Chem. Eng. Sci. 27 (1972) 1197–1203.
[39] G. Soave, S. Gamba, L.A. Pellegrini, SRK equation of state: predicting binary interaction parameters of hydrocarbons and related compounds, Fluid Phase Equilib. 299 (2010) 285–293.
[40] J.M. Prausnitz, R.N. Lichtenthaler, E.G. de Azevedo, Molecular thermodynamics of fluid-phase equilibria, Prentice Hall PTR, Englewood Cliffs, N.J., 1999.
[41] V. Giovangigli, L. Matuszewski, F. Dupoirieux, Detailed modeling of planar transcritical $H_2 - O_2 - N_2$ flames, Combust. Theor. Model. 15 (2011) 141–182.
[42] Y.V.C. Rao, Chemical engineering thermodynamics, Universities Press, 1997.
[43] J.F. Grcar, The Twopnt program for boundary value problems, Technical Report, Report No. SAND91-8230, Sandia National Laboratories, 1992.
[44] T. Lu, C.K. Law, A criterion based on computational singular perturbation for the identification of quasi steady state species: a reduced mechanism for methane oxidation with no chemistry, Combust. Flame. 154 (2008) 761–774.
[45] M. Chmielewski, M. Gieras, Planck mean absorption coefficients of H_2O, CO_2, CO and NO for radiation numerical modeling in combusting flows, J. Power Technol. 95 (2015) 97–104.
[46] B.E. Launder, D.B. Spalding, Lectures in mathematical models of turbulence, Academic Press Inc., New York, N.Y., 1972.
[47] L. Figura, A. Gomez, Laminar counterflow steady diffusion flames under high pressure ($p \leq 3$ MPa) conditions, Combust. Flame 159 (2012) 142–150.
[48] R. Holub, P. Voňka, The chemical equilibrium of gaseous systems, Springer, Netherlands, 1976.